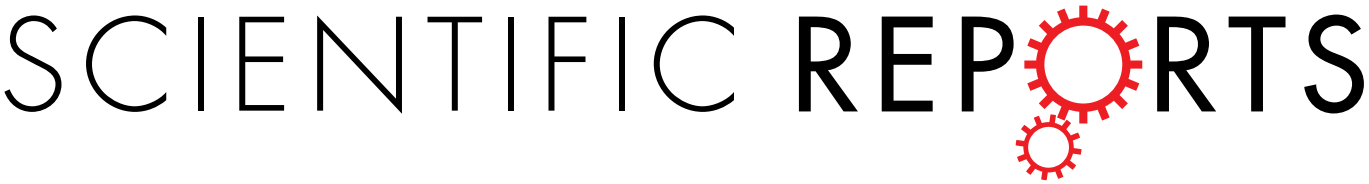

OPEN

Laser-Driven Ion Acceleration from Plasma Micro-Channel Targets

D. B. Zou[1,2], A. Pukhov[2], L. Q. Yi[2], H. B. Zhuo[1,3], T. P. Yu[1], Y. Yin[1] & F. Q. Shao[1]

Received: 03 October 2016
Accepted: 13 January 2017
Published: 20 February 2017

Efficient energy boost of the laser-accelerated ions is critical for their applications in biomedical and hadron research. Achiev-able energies continue to rise, with currently highest energies, allowing access to medical therapy energy windows. Here, a new regime of simultaneous acceleration of ~100 MeV protons and multi-100 MeV carbon-ions from plasma micro-channel targets is proposed by using a ~10^{20} W/cm^2 modest intensity laser pulse. It is found that two trains of overdense electron bunches are dragged out from the micro-channel and effectively accelerated by the longitudinal electric-field excited in the plasma channel. With the optimized channel size, these "superponderomotive" energetic electrons can be focused on the front surface of the attached plastic substrate. The much intense sheath electric-field is formed on the rear side, leading to up to ~10-fold ionic energy increase compared to the simple planar geometry. The analytical prediction of the optimal channel size and ion maximum energies is derived, which shows good agreement with the particle-in-cell simulations.

Laser-driven energetic ion beam has attracted great attention because of its significance in many research communities and industrial applications. Compared with the conventional accelerators, these beams can be generated over only a few micrometer distances, having shorter pulse duration and more sufficient intensities. Over the past two decades, several mechanisms for laser-driven ion acceleration have been studied theoretically and experimentally, including target normal sheath acceleration (TNSA)[1–3], radiation-pressure acceleration (RPA)[4–8], breakout afterburner acceleration (BOA)[9,10], and shock acceleration[11,12]. However, the maximum achieved energies[13,14] of ~85 MeV for protons and ~20 MeV/u for carbon-ions are still unmatched for the demand of the particular applications. For the current laser facilities, TNSA has been identified as one of the most robust mechanisms. In this regime, the sheath acceleration electric field, scales as[15] $E_{sheath} \propto (n_h T_h)^{1/2}$, is dependent on the hot-electron density n_h and temperature T_h. For a simple planar target, $J \times B$ heating[16] or vacuum heating[17] dominates the hot-electron generation, while the obtained hot-electrons are usually $k_B T_h < e\phi_p$ and $n_h < n_c$, in which k_B is the Boltzmann constant, $e\phi_p$ is the ponderomotive potential and n_c is the critical plasma density[18]. Many methods such as placing suitable-scale preplasma[19,20] and employing nanosphere surface[21–23] or microcone[24,25] has been suggested to heat the electrons. Nevertheless, simultaneously great increase of n_h and T_h remains a challenging endeavor. Recently, a micro-tube target has been identified to an usable method to achieve the light intensification for a $I \geq 10^{22}$ W/cm^2 laser intensity and thus increase the electron temperature T_h[26]. For $I < 10^{22}$ W/cm^2 being in the attainable domain of present laser conditions, it is found that the laser field is mainly depleted by the "dragged-out" electrons from the tube and loses the amplification effect[26]. The generated electron bunches, with extremely high densities and temperatures, are hopeful to act as externally injected hot-electron sources for TNSA and increase ionic energies dramatically.

In this article, we report on a considerable energy advancement of TNSA protons and carbon-ions by utilizing a ~10^{20} W/cm^2 modest intensity laser incident on a plasma micro-channel target (CT). The CT structure is composed of a preposed gold micro-channel and an attached plastic substrate. With the aid of two-dimensional (2D) particle-in-cell (PIC) simulations, we find that the overdense (far beyond n_c) electron sources with "superponderomotive" temperatures ($k_B T_h > e\phi_p$) are generated in the plasma channel. As the externally injected hot-electron sources, an intense sheath electric-field will be induced when they penetrate through the substrate, which sharply enhances ion acceleration. Hundreds of MeV protons and carbon-ions, almost one order of magnitude higher than that achieved using the usual planar target (PT), are simultaneously produced.

[1]College of Science, National University of Defense Technology, Changsha 410073, People's Republic of China. [2]Institut für Theoretische Physik I, Heinrich-Heine-Universität Düsseldorf, Düsseldorf, 40225 Germany. [3]IFSA Collaborative Innovation Center, Shanghai Jiao Tong University, Shanghai 200240, People's Republic of China. Correspondence and requests for materials should be addressed to A.P. (email: pukhov@tp1.uni-duesseldorf.de) or H.B.Z. (email: hongbin.zhuo@hotmail.com)

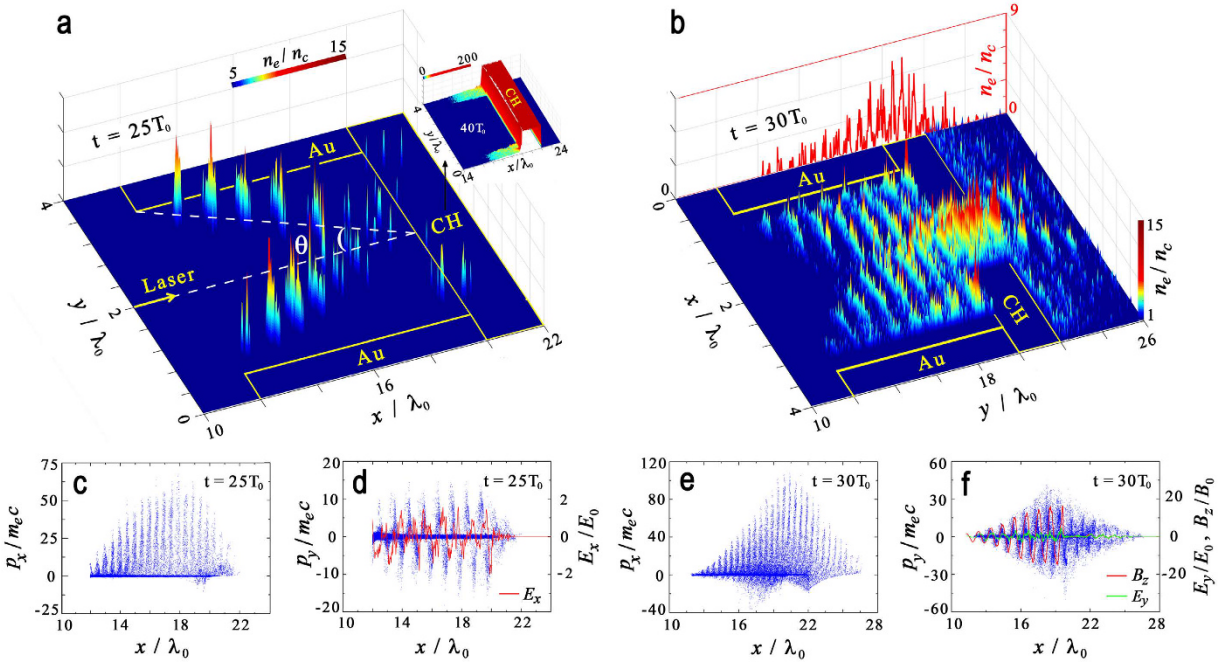

Figure 1. Snapshots of the interaction at $t = 25T_0$ and $30T_0$ showing the density of the Au-electron in the channel [(**a**) and (**b**)], the longitudinal [(**c**) and (**e**)] and transverse [(**d**) and (**f**)] momenta for the CT. Here, θ in panel (**a**) represents the angle between the electron trajectory and the laser axis, and the inset is the distribution of the CH-electron density; The flank in panel (**b**) plots the on-axis Au-electron density along the laser propagation direction; The red line in panel (**d**) gives the longitudinal electric-field E_x along the $y = 3.4\lambda_0$ direction excited in the channel. The lines in panel (**f**) are the on-axis magnetic-(B_z, red line) and electric-(E_y, green line) fields in the channel. $E_0 = m_e\omega_0 c/e$ and $B_0 = m_e\omega_0/e$.

Results

Numerical and theoretical modelling. To explore the dynamic of the laser interacting with the plasma micro-channel target, we have carried out 2D PIC simulations with the collision and ionization effects included. A p-polarized planar wave, with $\lambda_0 = 0.8\,\mu$m and $T_0 = 2.67$ fs being the laser wavelength and period, is perpendicularly incident into the plasma micro-channel along the laser axis. The laser pulse has a temporal profile of $a = eE_L/m_e\omega_0 c = a_0 \sin^2(\pi t/2\tau_0)$, where E_L is the laser electric field, $a_0 = 10$ is the normalized laser amplitude, and $\tau_0 = 10T_0$ is the pulse duration. This corresponds to a laser intensity of $\sim 2.14 \times 10^{20}$ W/cm^2, power of ~44 TW and total energy of ~1.2 J. The channel, of length $L_0 = 8.0\lambda_0$, wall-thickness $r_0 = 0.5\lambda_0$ and transverse interval $d_0 = 3.0\lambda_0$, is located between $x_0 = 12\lambda_0$ and $x_1 = 20\lambda_0$, attached directly to a plastic substrate layer of thickness $L_1 = 2.0\lambda_0$. We use weakly ionized gold (Au) and polystyrene plastic (CH) materials with realistic density 19.32 g/cm^3 and 1.05 g/cm^3, respectively. The initially ionic charge states of Au, H and C are set to $Z_i = 1$, 1 and 2, respectively. The corresponding dimensionless ion densities are $n_{Au^+} = 33.5n_c$ and $n_{H^+} = n_{C^{2+}} = 28.1n_c$.

Figures 1(a) and (b) present the density evolutions of the Au-electrons from the simulation. We can see that two trains of laminar electron pulses separated by a periodic length of $\sim 1\lambda_0$ are dragged out from the channel into the cavity by the laser. This effect can be attributed to breaking of the stimulated Langmuir oscillation for sufficiently large laser amplitudes[27]. Different from the Brunel mechanism[17], the "dragged-out" electrons are accelerated forward, instead of pushed back into the Au plasma. Meanwhile, owing to the transverse momenta [Fig. 1(d) and (f)], these bunches spread along the lateral direction and partially converge to the central region during propagation inside the channel. They then disperse radially after penetrating through the attached substrate. The electrons of the CH layer move in the opposite direction as a return current to neutralize the positive charged channel walls caused by these ejected electrons, as shown in the inset of Fig. 1(a). The "dragged-out" electrons from the channel are therefore responsible for inducing the rear accelerating field.

We establish a waveguide acceleration (WGA) model to examine the dynamic of the "dragged-out" electrons inside the channel. As the laser propagates through the plasma waveguide channel, the longitudinal electric-field that arises from the waveguide transverse magnetic (TM$_{nm}$) mode can be excited to accelerate the electrons with a proper phase ($E_x^{\mathrm{TM}} < 0$)[28,29]. In the 2D planar geometry, the channel has an unlimited z-direction width ($d_1 \to \infty$). The longitudinal and transverse electric-fields in the channel can be expressed as

$$E_x = A_0 \sin(k_y y) e^{ik_x x - \omega_0 t}, \quad (1)$$

$$E_y = \frac{ik_x k_y}{k^2 - k_x^2} A_0 \cos(k_y y) e^{ik_x x - \omega_0 t}, \tag{2}$$

where A_0 is a constant, $k_y = n\pi/d_0$, $k_x^2 = k^2 - k_y^2$, and $k = 2\pi/\lambda_0$ is the wave number of the incident laser. We can roughly calculate the amplitude of the longitudinal electric-field by $E_x^{\mathrm{TM}} \simeq E_L \left| E_x/E_y \right| = E_L/(4d_0^2/n^2\lambda_0^2 - 1)^{1/2}$. The maximum momentum gains from this field depend on the dephasing time $t_d = 2\lambda_0/(v_{ph} - c)$ and the acceleration time t_a, where $v_{ph} \simeq (1 + \lambda_0^2/8d_0^2)c$ is the laser phase velocity as only the lowest TM_{01} mode is considered for a small d_0. The acquired momentum can therefore be estimated to be $p_x^{\mathrm{TM}} = e\overline{E}_x^{\mathrm{TM}} \cdot \min(t_d, t_a)$, where $\overline{E}_x^{\mathrm{TM}} \simeq E_x^{\mathrm{TM}}/2$ is the averaged accelerating field. For these "dragged-out" electrons, they turn to the forward direction by the ev_yB_z force and can be further accelerated by the eE_x^{TM} force. Besides, the effect of superluminous phase velocity ($v_{ph} > c$) in the plasma waveguide channel should also be considered for a wave with its amplitude exceeding the critical value $a_{cr} = [2c/(v_{ph} - c)]^{1/2}$. Following the work[30] of Robinson *et al.*, the electron longitudinal momentum can be rewritten as

$$\frac{p_x}{m_e c} = \frac{a^2}{2} + \frac{p_x^{\mathrm{TM}}}{m_e c} \quad (a < a_{cr}), \tag{3}$$

$$\frac{p_x}{m_e c} = \frac{a}{(v_{ph}^2/c^2 - 1)^{1/2}} + \frac{p_x^{\mathrm{TM}}}{m_e c} \quad (a \geq a_{cr}). \tag{4}$$

Here, the first terms of the right-hand sides of Eqs (3) and (4) are the contributions from the ponderomotive force, and the second ones denote that of the longitudinal electric-field acceleration. Using $dp_y/dt = eE_y + ev_xB_z$ (essentially, $E_y \simeq cB_z$ and $v_x \simeq c$), one can immediately obtain the transverse momentum $p_y/m_e c \simeq 2a$. Although E_y almost decreases to zero because the half-wave loss occurs while the laser are reflected by the attached CH-layer at $t = 30T_0$, B_z approaches a 2-fold enhancement due to the change of the light wave-vector direction and thus keep $E_y + cB_z$ constant, as shown in Fig. 1(f). Taking $a = a_0$ and $t_a = \tau_0$, this gives $v_{ph} \simeq 1.014c$, $a_{cr} \simeq 12$, $eE_x^{\mathrm{TM}}/m_e\omega_0 c \simeq 1.7$, $p_y/m_e c \simeq 20$ and $p_x/m_e c \simeq 103$. This field amplitude and the momenta show fair consistence with our simulation results in Fig. 1(d)–(f).

The maximum electron momenta from Eqs (3)–(4) and $p_y/m_e c \simeq 2a_0$ are shown in Fig. 2(a) in a wide laser intensity range, which are in agreement with the simulations. We find that p_x scales as a_0 for $a_0 \geq a_{cr}$, which is different from $p_x \propto a_0^2$ in the case of $a_0 < a_{cr}$. Due to the fact that $3k_B T_h/2 = \overline{\gamma} m_e v_e^2/2$, the electron temperature can be simplified to $k_B T_h \simeq p_x m_e c^2/6$, where $\overline{\gamma} \simeq (1 + p_x^2 + p_y^2)^{1/2}/2 \simeq p_x/2$ is the averaged electron energy since $p_x^2 \gg p_y^2 \gg 1$ and $v_e \simeq c$ provided the "dragged-out" electrons become fully thermalized. Therefore, we have

$$k_B T_h = a_0 \cdot m_e c^2 [2\sqrt{2}\, d_0/\lambda_0 + \pi c\tau_0/\sqrt{4d_0^2 - \lambda_0^2}]/6 \ (a_0 \geq a_{cr}), \tag{5}$$

Considering $T_h \propto p_x \propto a_0^2$ for $a_0 < a_{cr}$, we obtain

$$k_B T_h = \zeta a_0^2 \cdot m_e c^2 \ (a_0 < a_{cr}), \tag{6}$$

where the proportion coefficient ζ can be solved from the continuity of Eqs (5) and (6) at $a_0 = a_{cr}$. For above given d_0 and τ_0, it is approximated to $k_B T_h \simeq 2a_0 \cdot m_e c^2$ for $a_0 \geq a_{cr}$ and $k_B T_h \simeq (2a_0^2/a_{cr}) \cdot m_e c^2$, respectively. Taking $a_0 = 10$, we have $k_B T_h \simeq 8.5$ MeV roughly equal to the PIC result 9.1 MeV in Fig. 2(b), which is well above the PT case. Figure 2(c) shows that the theoretical results from Eqs (5)-(6) agree well with the simulations. The temperatures for the CTs are very high, almost twice the Wilks's ponderomotive potential[1] $k_B T_h/m_e c^2 = (1 + a_0^2)^{1/2} - 1$. We also notice that the PT results are very low, but in accordance with the Haines's relativistic model[31] $k_B T_h/m_e c^2 = (1 + 2^{1/2} a_0)^{1/2} - 1$ and Beg's experimental fitting[32] $k_B T_h/m_e c^2 \sim 0.47 a_0^{2/3}$. This is due to the fact that the electrons cannot receive all energy from the ponderomotive potential[31]. Further, the sequential ionization of C^{6+} ions which will reduce the electron temperature is correctly modeled in our simulations. Note that most of the "dragged-out" electron bunches typically have a transverse extent of $l_t \sim cT_0 = 1\lambda_0$[33]. Due to the charge conservation, assuming that all skin-layer electrons are extracted, the hot-electron density can be estimated to

$$\frac{n_h}{n_c} \simeq \kappa \frac{n_e^{Au}}{n_c} \frac{l_s}{l_t} = \frac{a_0^{0.9}}{2\pi} \sqrt{\frac{n_e^{Au}}{n_c}}, \tag{7}$$

where $\kappa = a_0^{0.4}$ is the ionization modified coefficient[34], $l_s = (a_0 n_c/n_e^{\mathrm{Au}})^{1/2}/2\pi$ is the skin depth and $n_e^{\mathrm{Au}} = n_{\mathrm{Au}^{+}}$. Figure 1(b) [red line] gives that the maximum on-axis electron density at $t = 30T_0$ is as high as $\sim 7.5n_c$, which is comparable to $n_h \simeq 7.3n_c$ obtained from Eq. (7). As shown in Fig. 2(a) (blue line), the highest density of the "dragged-out" electron bunches shows consistent with the simulations and is far beyond the results observed in other works[18] ($< 1n_c$). The on-axis profile of the quasi-static electric field E_x at $t = 30T_0$ is depicted in Fig. 2(d). Driven by these dense energetic electron bunches, the accelerating electric-field strength is about 36 TV/m high, and the acceleration region is broadened, both of which are very beneficial for the subsequent ion acceleration.

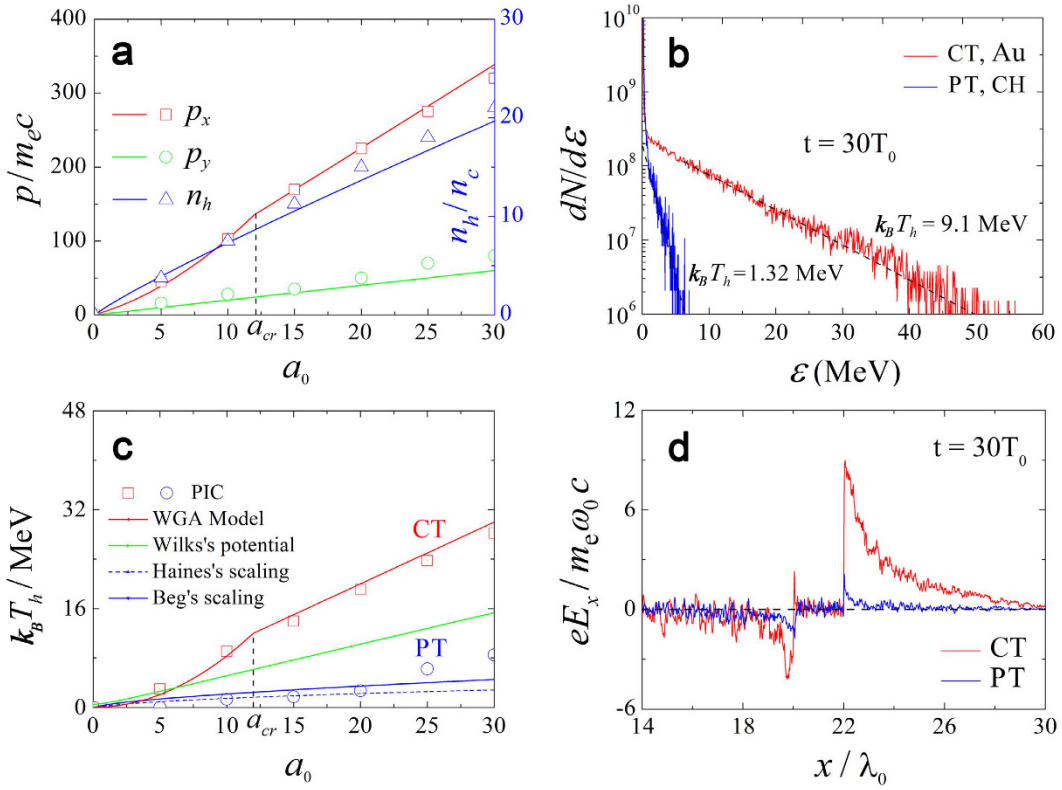

Figure 2. (**a**) The maximum transverse and longitudinal momenta and the highest axial density of the "dragged-out" electrons along the central axis at $t = 30T_0$ versus laser amplitude a_0 for the CT case. (**b**) Spectra of the Au- (CT) and CH- (PT) electrons at $t = 30T_0$ for both cases. The electron temperatures are labeled around the curves. (**c**) The highest Au-electron temperature versus laser amplitude a_0 obtained from the WGA model and PIC simulations. (**d**) The axial profile of the longitudinal electric-field E_x along the axis $y = 2.0\lambda_0$ at $t = 30T_0$

Besides, the laser energy is also absorbed more effectively, resulting in a high laser-to-electron conversion efficiency of ~54% in contrast to ~12% of the PT case as shown in Fig. 3(a).

For ultrashort ultra-intense laser pulses, field ionization becomes significant compared to collisional ionization[35]. Figure 3(b) shows that the averaged charge state of the Au ions grows exponentially as soon as the laser impinges on the channel. The final ionization degree approaches 56, consistent with $Z_i = 58$ calculated by the Ammasov-Delone-Krainov (ADK) model[36]. This corresponds to an extremely high electron density of $\sim 2000n_c$, which is typically difficult to be modeled using traditional PIC simulations. On the other hand, nearly all carbon-ions are immediately ionized to the 6th ionic charge state due to relatively low ionization threshold. The spectral distributions of protons and C^{6+} ions at $t = 80T_0$ are presented in Fig. 3(c) and (d). As expected, high energies, up to 33 MeV for protons and 127 MeV for C^{6+} ions, are simultaneously observed. Surprisingly this is almost an order of magnitude larger than that in the planar geometry, where the maximum energy only reaches 5 MeV for protons and 28 MeV for carbon-ions. Consequently, the energy conversion efficiency from laser to ions is increased to ~7.4% from ~1.56% of the PT case as shown in Fig. 3(a). Similar to previously reported results[37–40], the protons are accelerated preferentially to heavier carbon-ions. The latter behaves as a buffer to optimize the spectral profiles of the protons, leading to the appearance of the pronounced quasi-monoenergetic peaks with central energies 17 MeV and 1 MeV for both cases, respectively. As a result, the carbon-ion spectra have a typical Maxwellian distribution with cutoff energies.

Ion energy scaling. We next extend the laser intensity range to obtain the scaling laws of the maximum energies. According to the model of a two-species plasma expansion[41], the maximum electric-field beyond the heavy-ion front can be simplified to

$$E_x(t) = \frac{\sqrt{2}k_BT_h}{e\lambda_{D,f}}\left[1 + \frac{x_L - x_H}{\sqrt{2}\lambda_{D,f}}\right]^{-1}, \tag{8}$$

where $\lambda_{D,f} = (T_h/4\pi n_h e^2)^{1/2}$ is the hot-electron Debye length, and x_L, x_H are the positions of the light- and heavy-ion fronts, respectively. These can be calculated as $x_{L(H)} = c_{s,L(H)}t[2\ \ln \omega_{pL(H)}t - 1]$, where $c_{s,L(H)} = [Z_{L(H)}T_h/m_{L(H)})]^{1/2}$ is the ion acoustic velocity, $Z_{L(H)}$ and $m_{L(H)}$ are the ionic charge and mass, $\omega_{pL(H)} = [4\pi Z_{L(H)}n_{e0,L(H)}e^2/m_{L(H)}]^{1/2}$ is the ion plasma frequency, $n_{e0,L(H)} = Z_{L(H)}n_{L(H)}$ and $n_{L(H)}$ are the initial ion

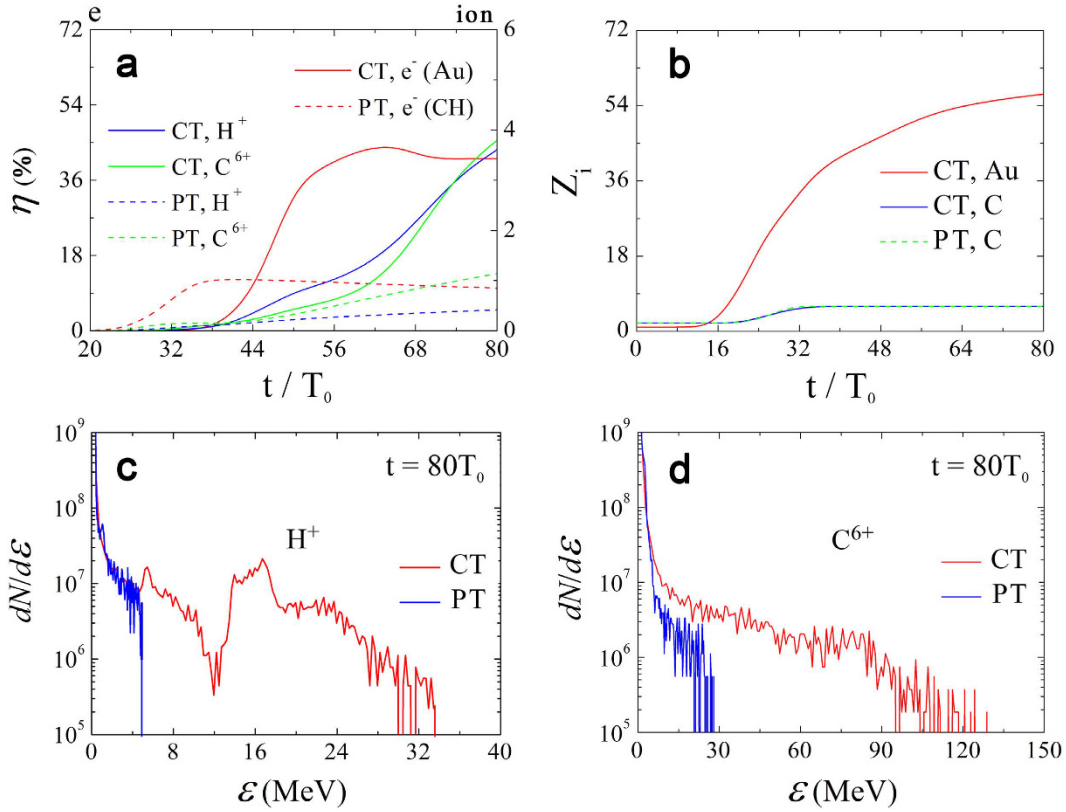

Figure 3. Temporal evolution of (**a**) the energy conversion efficiencies from laser to particles and (**b**) the average ionization degrees of the Au- and carbon-ions. Spectra of (**c**) protons and (**d**) carbon ions at $t = 80T_0$.

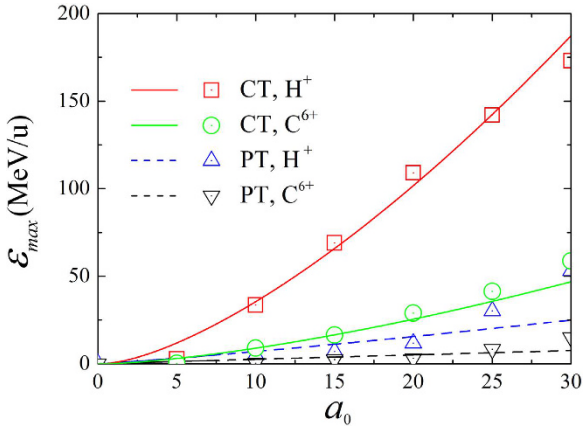

Figure 4. Scaling of the maximum proton and carbon-ion energies at $t = 80T_0$ versus laser amplitude a_0 from the integral of Eq. (8) (lines) and simulations (symbols).

densities, where the subscripts L(H) correspond to the light- (heavy-) ions. By integrating the light-ion equation of motion in this field, we can obtain the maximum light-ion momentum, $p_{\max,L} = \int_0^t eE_x(t)dt$, and energy, $\varepsilon_{\max,L} = p^2_{\max,L}/2m_L$, as a function of time. For the sake of simplicity, the maximum heavy-ion energy is estimated by multiplying a factor $\alpha \sim m_L Z_H^2/m_H Z_L^2$ from the hybrid-Boltzmann-Vlasov-Poisson model[39], i.e., $\varepsilon_{\max,H} \simeq \alpha\varepsilon_{\max,L}$. Figure 4 gives the maximum energies of protons and C^{6+} ions per nucleon in simulations over currently achievable intensities, which grow almost exponentially and show a good agreement with the above analytical model. Furthermore, the results demonstrate that the presence of the metal channel can achieve about 10-fold enhancement of energies for both ion species. With a laser intensity ~10^{21} W/cm^2 ($a_0 = 25$), the highest energies are close to 150 MeV for protons and 42 MeV/u (~500 MeV) for C^{6+} ions, which are in the typical energy window of tumor therapy[42].

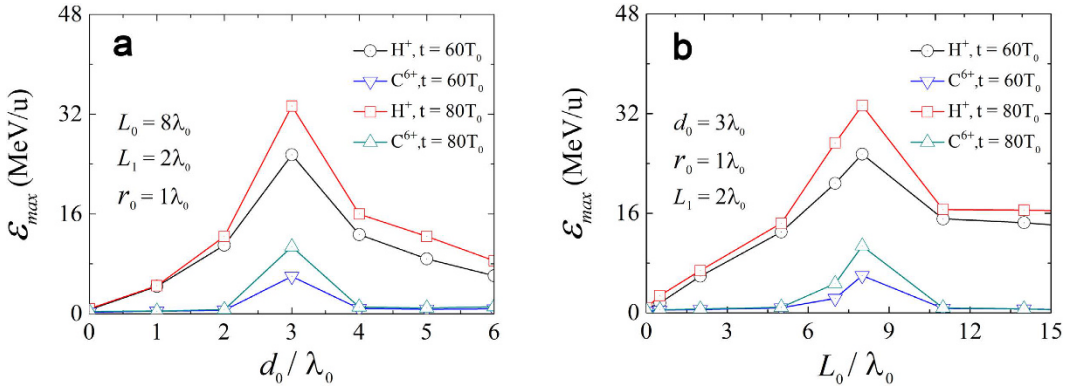

Figure 5. The maximum proton and carbon-ion energies per nucleon as a function of (**a**) the spatial interval d_0 and (**b**) length L_0 at $t = 60T_0$ and $t = 80T_0$ for the CTs, respectively.

The optimal channel size for the experimental design. To achieve efficient ion acceleration, an important condition is that these "dragged-out" electron bunches can be focused at the central region of the CH-layer front surface. This requires that the angle $\theta \simeq \arctan(p_y/p_x)$ as illustrated in Fig. 1(a) is comparable to the optimum angle $\theta_0 = \arctan(d_0/2L_0)$. For the above case, $\theta \simeq 11^\circ$ is very close to $\theta_0 \simeq 10.6^\circ$, leading to optimal focusing as displayed in Fig. 1(b). The angle matching also provides us with a design method of the optimal channel size, i.e., the relationship $L_0 \simeq (p_x/2p_y)d_0$ should be satisfied. The parametric influence of the length L_0 and the spatial interval d_0 on the maximum ion energies is shown in Fig. 5. One note that the maximum energies of protons and C^{6+} ions are the highest when the spatial interval d_0 is equal to $3\lambda_0$. The reason is that when d_0 is very small, the earlier "dragged-out" electrons blocking the channel entrance prevent the laser from propagating into the channel; conversely if d_0 is too large, it is difficult for these electron bunches to focus at the CH-layer front surface. Different from the nanostructured-attached targets, where surface plasmon resonance excitation[43] or multipass stochastic heating[44] may be excited to strength the laser absorption, a proper channel length is essential in our proposed mechanism. If the length of the channel is too short, the laser cannot throw up enough "dragged-out" electron bunches since they have a typical spacing of $1\lambda_0$; whereas if it is too long, early defocusing will weaken the subsequent acceleration. There therefore exists an optimal length $L_0 = 8.0\lambda_0$ as seen in Fig. 5(b), which is in accordance with the above predicted $L_0 = d_0/2 \tan \theta \simeq 7.7\lambda_0$.

Discussion

In the past decade, a large amount of efforts have been dedicated to the research into the boost of ion beam energies, such as using undersense or near-critical density plasmas[19,20,45], porous-structured-films[21,22,23], and micro-tubes[25,26]. Most of these schemes are based on the improvement of the hot electron temperature. For instance, the direct laser acceleration (DLA)[46,47] in the undersense plasmas is a very effective mechanism to heat the electrons and then improve the ion energies. In the DLA mechanism, the electron temperature scales as the laser amplitude[46], i.e., $T_h \sim 1.5a_0$, which is comparable to our scheme. However, it is known that the sheath electric-field in TNSA is proportional to the square root of $n_h T_h$, and simultaneously great increase of n_h and T_h is therefore vital to significantly increase the ion energies. Benefiting from high-density high-temperature electron bunches dragged from the channel, the energy gain in our scheme is much higher than that in these enhanced TNSA schemes[21,22,23,45,48] based on the DLA and other methods. As a result, the total laser energy (only 1.2 J in our scheme) is far below ~50 J in the previous works[45,48] to generate multi-100 MeV ions. Besides, the direct laser acceleration (DLA) of the electrons essentially depends on the laser pulse propagating in infinitely homogeneous plasmas. In contrast, the mode conversion from the electromagnetic (EM) mode of the laser to the transverse magnetic (TM) mode occurs in the case of laser propagating in a waveguide channel. A longitudinal electric field of the EM mode is excited in the channel, which plays a crucial role in the acceleration.

Here, plasma micro-channel target is used to provide the overdense hot-electron bunches with "superponderomotive" temperatures. After being accurately focused with a proper channel size, they penetrate through the attached plastic substrate to induce a strong sheath electric-field. Compared with the usual planar targets, a ~10 times energy boost of protons and carbon ions is achieved. The optimal channel size and the ion energy scaling are obtained from the analytical model and are confirmed by simulations. This method offers possibilities to obtain hundreds of MeV proton and carbon-ion beams suitable with the present laser facilities.

Methods

Numerical simulations. For high-Z target materials, PIC simulations in previous works generally set an averaged ionization degree, forming a fixed electron density for simplicity; moreover, reduced target density is also assumed owing to limited computational resources. One note that the highest electron density reaches $n_e^{Au} = 2646.5n_c$ and $n_e^{CH} = 196.7n_c$ for completely ionized Au and CH materials, which is far beyond the capability of the available high performance computers. To solve this problem, a Voronoi particle merging algorithm[49] has been implemented in the code VLPL[50], which effectively controls the excessively increasing simulated particle numbers due to the sequential ionization. In our simulation, the simulation box is $x \times y = 48\lambda_0 \times 4\lambda_0$ with a cell

size of $0.02\lambda_0 \times 0.02\lambda_0$ and a time step $\Delta t = 0.002T_0$. We use 32 macroparticles per cell and initially cold plasmas. For both particles and fields, we used the periodic boundary conditions.

References

1. Wilks, S. C. *et al.* Energetic proton generation in ultra-intense laser solid interactions. *Phys. Plasmas* **8,** 542 (2001).
2. Pukhov, A. Three-Dimensional Simulations of Ion Acceleration from a Foil Irradiated by a Short-Pulse Laser. *Phys. Rev. Lett*. **86,** 3562 (2001).
3. Hegelich, B. M. *et al.* Laser acceleration of quasi-monoenergetic MeV ion beams. *Nature (London)* **439,** 441–444(2006).
4. Macchi, A. *et al.* Laser Acceleration of Ion Bunches at the Front Surface of Overdense Plasmas. *Phys. Rev. Lett* **94,** 165003(2005).
5. Robinson, A. P. L. *et al.* Radiation pressure acceleration of thin foils with circularly polarized laser pulses. *New J. Phys*. **10,** 013021(2008).
6. Yan, X. Q. *et al.* Generating High-Current Monoenergetic Proton Beams by a Circularly Polarized Laser Pulse in the Phase-Stable Acceleration Regime. *Phys. Rev. Lett* **100,** 135003(2008).
7. Qiao, B. *et al.* Stable GeV Ion-Beam Acceleration from Thin Foils by Circularly Polarized Laser Pulses. *Phys. Rev. Lett* **102,** 145002(2009).
8. Kar, S. *et al.* Ion Accelerationin Multispecies Targets Driven by Intense Laser Radiation Pressure. *Phys. Rev. Lett* **109,** 185006(2012).
9. Yin, L. *et al.* GeV laser ion acceleration from ultrathin targets: The laser break-out afterburner. *Laser Part. Beams* **24,** 291(2008).
10. Yin, L. *et al.* Monoenergetic and GeV ion acceleration from the laser breakout afterburner using ultrathin targets. *Phys. Plasmas* **14,** 056706(2007).
11. Haberberger, D. *et al.* Collisionless shocks in laser-produced plasma generate monoenergetic high-energy proton beams. *Nature Phys*. **8,** 95–99(2012).
12. Silva, L. O. *et al.* Proton Shock Acceleration in Laser-Plasma Interactions. *Phys. Rev. Lett* **92,** 015002(2004).
13. Wagner, F. *et al.* Maximum Proton Energy above 85 MeV from the Relativistic Interaction of Laser Pulses with Micrometer Thick CH^2 Targets. *Phys. Rev. Lett* **116,** 205002(2016).
14. Bin, J. H. *et al.* Ion Acceleration Using Relativistic Pulse Shaping in Near-Critical-Density Plasma. *Phys. Rev. Lett* **115,** 064801(2015).
15. Mora, P. Plasma Expansion into a Vacuum, *Phys. Rev. Lett*. **90,** 185002 (2003).
16. Kruer, W. L. *et al.* J×B heating by very intense laser light. *Phys. Fluids* **28,** 430 (1985).
17. Brunel, F. Not-So-Resonant, Resonant Absorbtion. *Phys. Rev. Lett*. **59,** 52 (1987).
18. Macchi, A. *et al.* Ion acceleration by superintense laser-plasma interaction. *Rev. Mod. Phys*. **85,** 751 (2013).
19. Zheng, F. L. *et al.* Preplasma effects on the generation of high-energy protons in ultraintense laser interaction with foil targets. *Phys. Plasmas* **20,** 123105 (2013).
20. Zou, D. B. *et al.* Enhanced target normal sheath acceleration based on the laser relativistic self-focusing. *Phys. Plasmas* **21,** 063103 (2014).
21. Margarone, D. *et al.* Laser-Driven Proton Acceleration Enhancement by Nanostructured Foils. *Phys. Rev. Lett*. **109,** 234801 (2012).
22. Zigler, A. *et al.* Enhanced Proton Acceleration by an Ultrashort Laser Interaction with Structured Dynamic Plasma Targets. *Phys. Rev. Lett*. **110,** 215004 (2013).
23. Dalui, M. *et al.* Bacterial cells enhance laser driven ion acceleration. *Sci. Rep*. **4,** 6002 (2014).
24. Gaillard, S. A. *et al.* Increased laser-accelerated proton energies via direct laser-light-pressure acceleration of electrons in microcone targets. *Phys. Plasmas* **18,** 056710(2011).
25. Kluge, T. *et al.* High proton energies from cone targets electron acceleration mechanisms. *New J. Phys* **14,** 023038(2012).
26. Ji, L. L. *et al.* Towards manipulating relativistic laser pulses with micro-tube plasma lenses. *Sci. Rep*. **6,** 23256 (2016).
27. Naumova, N. *et al.* Attosecond Electron Bunches. *Phys. Rev. Lett*. **93,** 195003 (2004).
28. Shen, H. M. Plasma waveguide A concept to transfer electromagnetic energy in space. *J. Appl. Phys*. **69,** 6827 (1991).
29. Yi, L. Q. *et al.* Bright X-Ray Source from a Laser-Driven Microplasma Waveguide. *Phys. Rev. Lett*. **116,** 115001 (2016).
30. Robinson, A. P. L. *et al.* The effect of superluminal phase velocity on electron acceleration in a powerful electromagnetic wave. *Phys. Plasmas* **22,** 083114 (2015).
31. Haines, M. G. *et al.* Hot-Electron Temperature and Laser-Light Absorption in Fast Ignition. *Phys. Rev. Lett*. **102,** 045008 (2009).
32. Beg, F. N. *et al.* A study of picosecond laser solid interactions up to 10^9 Wcm^{-2}. *Phys. Plasmas* **4,** 447 (1997).
33. Ma, Y. Y. *et al.* Dense quasi-monoenergetic attosecond electron bunches from laser interaction with wire and slice targets. *Phys. Plasmas* **13,** 110702 (2006).
34. Braenzel, J. *et al.* Coulomb-Driven Energy Boost of Heavy Ions for Laser-Plasma Acceleration. *Phys. Rev. Lett*. **114,** 124801 (2015).
35. Hegelich, M. *et al.* MeV Ion Jets from Short-Pulse-Laser Interaction with Thin Foils. *Phys. Rev. Lett*. **89,** 085002 (2002).
36. Ammosov, M. *et al.* Tunnel Ionization of complex atoms and of atomic ions in an alternating electromagnetic field. *Sov. Phys. JETP* **64 ,**1191 (1986).
37. Kovalev, V. F. *et al.* Analytic Solutions to the Vlasov Equations for Expanding Plasmas. *Phys. Rev. Lett* **90,** 185004 (2003).
38. Tikhonchuk, V. T. *et al.* Ion acceleration in short-laser-pulse interaction with solid foils. *Plasma Phys. Control. Fusion* **47,** B869 (2005).
39. Bochkarev, S. G. *et al.* Investigation of Ion Acceleration in an Expanding Laser Plasma by Using a Hybrid Boltzmann-Vlasov-Poisson Model. *Plasma Phys. Rep*. **32,** 205 (2006).
40. Yu, T. P. *et al.* Stable Laser-Driven Proton Beam Acceleration from a Two-Ion-Species Ultrathin Foil. *Phys. Rev. Lett* **105,** 065002 (2010).
41. Robinson, A. P. L. *et al.* Effect of Target Composition on Proton Energy Spectra in Ultraintense Laser-Solid Interactions. *Phys. Rev. Lett*. **96,** 035005 (2006).
42. Salamin, Y. I. *et al.* Direct High-Power Laser Acceleration of Ions for Medical Applications. *Phys. Rev. Lett*. **100,** 155004 (2008).
43. Ceccotti, T. *et al.* Evidence of Resonant Surface-Wave Excitation in the Relativistic Regime through Measurements of Proton Acceleration from Grating Targets. *Phys. Rev. Lett*. **111,** 185001 (2013).
44. Breizman, B. N. *et al.* Nonlinear physics of laser-irradiated microclusters. *Phys. Plasmas* **12,** 056706 (1999).
45. Wang, H. Y. *et al.* Efficient and stable proton acceleration by irradiating a two-layer target with a linearly polarized laser pulse. *Phys. Plasmas* **20,** 013101 (2013).
46. Gahn, G. *et al.* Multi-MeV Electron Beam Generation by Direct Laser Acceleration in High-Density Plasma Channels. *Phys. Rev. Lett*. **83,** 4772 (1999).
47. Pukhov, A. *et al.* Particle acceleration in relativistic laser channels. *Phys. Plasmas* **6,** 2847 (1999).
48. Liu, J. L. *et al.* Two-stage acceleration of protons from relativistic laser-solid interaction. *Phys. Rev. STAB* **15,** 101301 (2012).
49. Luu, Phuc T. *et al.* Voronoi Particle Merging Algorithm for PIC Codes. *Comput. Phys. Comm*. **202,** 165 (2016).
50. Pukhov, A. Three-dimensional electromagnetic relativistic particle-in-cell code VLPL (Virtual Laser Plasma Lab). *J. Plasma Phys*. **61,** 425 (1999).

Acknowledgements

We thank L. L. Ji, J. Farmer and Phuc T. Luu for the fruitful discussion, language editing and the help from the VLPL code, respectively. This work is supported by EUCARD-2, Deutsche Forschungsgemeinschaft SFB

TR18. D. B. Z. acknowledges financial support from the China Scholarship Council (CSC), the National Natural Science Foundation of China (11375265, 11474360, 11475259, 11622547 and 11675264), the Science Challenge Project (JCKY2016212A505), the National Basic Research Program of China (Grant No. 2013CBA01504), and the Research Project of NUDT (JQ14-02-02).

Author Contributions

D.B.Z. wrote the paper with contributions from H.B.Z. D.B.Z. performed the numerical simulations and theoretical analysis in collaboration with A.P. All authors (D.B.Z., A.P., L.Q.Y., H.B.Z., T.P.Y., Y.Y. and F.Q.S.) contributed to the manuscript preparation.

Additional Information

Competing financial interests: The authors declare no competing financial interests.

How to cite this article: Zou, D. B. *et al.* Laser-Driven Ion Acceleration from Plasma Micro-Channel Targets. *Sci. Rep.* **7**, 42666; doi: 10.1038/srep42666 (2017).

Publisher's note: Springer Nature remains neutral with regard to jurisdictional claims in published maps and institutional affiliations.

This work is licensed under a Creative Commons Attribution 4.0 International License. The images or other third party material in this article are included in the article's Creative Commons license, unless indicated otherwise in the credit line; if the material is not included under the Creative Commons license, users will need to obtain permission from the license holder to reproduce the material. To view a copy of this license, visit http://creativecommons.org/licenses/by/4.0/

© The Author(s) 2017

SCIENTIFIC REPORTS

OPEN

Erratum: Laser-Driven Ion Acceleration from Plasma Micro-Channel Targets

D. B. Zou, A. Pukhov, L. Q. Yi, H. B. Zhuo, T. P. Yu, Y. Yin & F. Q. Shao

Scientific Reports 7:42666; doi: 10.1038/srep42666; published online 20 February 2017; updated on 23 March 2017

The original version of this Article contained a typographical error in the spelling of the author H. B. Zhuo, which was incorrectly given as H. B. Zhou. This has now been corrected in the PDF and HTML versions of the Article.

This work is licensed under a Creative Commons Attribution 4.0 International License. The images or other third party material in this article are included in the article's Creative Commons license, unless indicated otherwise in the credit line; if the material is not included under the Creative Commons license, users will need to obtain permission from the license holder to reproduce the material. To view a copy of this license, visit http://creativecommons.org/licenses/by/4.0/

© The Author(s) 2017